PCCP

PAPER

Oxygen activation and CO oxidation over size-selected Pt$_n$/alumina/Re(0001) model catalysts: correlations with valence electronic structure, physical structure, and binding sites†

F. Sloan Roberts, Matthew D. Kane, Eric T. Baxter and Scott L. Anderson*

Oxidation of CO over size-selected Pt$_n$ clusters (n = 1, 2, 4, 7, 10, 14, 18) supported on alumina thin films grown on Re(0001) was studied using temperature-programmed reaction/desorption (TPR/TPD), X-ray and ultraviolet photoelectron spectroscopy (XPS/UPS), and low energy ion scattering spectroscopy (ISS). The activity of the model catalysts was found to vary by a factor of five with deposited Pt$_n$ size during the first reaction cycle (TPR) and by a factor of two during subsequent cycles, with Pt$_2$ being the least active and Pt$_{14}$ the most active. The limiting step in the reaction appears to be the binding of oxygen; however, this does not appear to be an activated process as reaction is equally efficient for 300 K and 180 K oxidation temperatures. Size-dependent shifts in the valence band onset energy correlate strongly with CO oxidation activity, and there is also an apparent correlation with the availability of a particular binding site, as probed by CO TPD. The morphology of the clusters also becomes more three dimensional over the same size range, but with a distinctly different size-dependence. The results suggest that both electronic structure and the availability of particular binding sites control activity.

Introduction

Fundamental research in heterogeneous catalysis focuses on answering the basic question of what controls catalyst reactivity. It is well known that different noble metals catalyze reactions differently in terms of efficiency, selectivity, *etc.*, but varying the size of the metal clusters can also play an important role in the catalyst behavior.[1–6] A useful approach to separating out the interrelated influences of the many parameters that govern realistic catalysts is preparation of "model" catalysts where parameters can be varied more independently. Model catalysts typically consist of small noble metal clusters (ideally with a narrow size distribution) supported on a well characterized single crystal or thin film support. Such systems allow standard surface analysis techniques to be used to determine attributes of the catalyst such as the location of binding/active sites, the physical/electronic structure of the clusters, *etc.*

There have been many studies of the catalytic activity of Pt group metals, including both applied[7–15] and fundamental[1,3,15–31] research, and a great deal is known about reaction mechanisms under a variety of conditions. Nonetheless, questions remain,

including the nature of the active sites present on very small particles. Our group and others have shown that metal clusters in the size range below 1 nm exhibit interesting and unexpected catalytic behavior, sometimes with improved catalytic activity compared to the bulk metal.[4,6,16,19,21,24,32–43] The CO oxidation reaction has been extensively studied under a wide variety of conditions[12,14,44–61] and thus provides a wealth of data to help understand the size-dependent results.

We previously observed that fluctuations in core level binding energies for Pd clusters supported on TiO$_2$(110) were correlated with the activity for the CO oxidation reaction.[6] Additional work on the same system suggested that oxidation was an activated process and that the electronic structure–activity correlation probably reflected electronic effects on the oxygen activation process.[36] We recently observed[39] a similar size-dependent correlation between core level binding energies and aqueous electrochemical activity for Pt$_n$/glassy carbon, which appeared to suggest a more general trend relating electronic structure to oxidation catalytic activity, however, more examples are needed to test this hypothesis.

Here we report a CO oxidation study of a series of model catalysts consisting of small Pt$_n$ (n = 1, 2, 4, 7, 10, 14, 18) clusters supported on thin alumina films grown on Re(0001). Controlling the size of the noble metal catalyst with atomic resolution allows us to investigate how even the smallest size changes affect catalyst activity. X-Ray/ultraviolet photoelectron spectroscopy (XPS/UPS) were used to determine the electronic

Department of Chemistry, University of Utah, 315 South 1400 East, Room 2020, Salt Lake City, UT 84112-0850, USA. E-mail: anderson@chem.utah.edu

† Electronic supplementary information (ESI) available: Raw ISS data, 180 K TPR results, $^{13}CO_2$ signal *vs.* cluster size, 180 K and 300 K integrated intensities for CO$_2$ and residual CO, and typical TPR sequences for Pt$_4$ and Pt$_{14}$. See DOI: 10.1039/c4cp02083a

This journal is © the Owner Societies 2014

Phys. Chem. Chem. Phys., 2014, **16**, 26443–26457 | **26443**

structure of the alumina film and the Pt_n clusters, temperature-programmed reaction/desorption (TPR/TPD) was used to study activity and determine the availability and density of binding sites, and low energy ion scattering was used to probe size-dependent cluster morphology.

Experimental methodology

The ultrahigh vacuum (UHV) chamber (base pressure $< \sim 2 \times 10^{-10}$ Torr) and cluster deposition beamline have been described previously.[32,62] Briefly, the UHV chamber allows for *in situ* sample preparation and is equipped with several surface analysis techniques such as mass spectrometry for temperature-programmed reaction/desorption (TPR/TPD), low energy ion scattering (ISS), X-ray photo-electron spectroscopy (XPS), and ultraviolet photoelectron spectroscopy (UPS). Our model catalyst is constructed on a rhenium(0001) single crystal (Marketech International) that is attached to a liquid nitrogen-cooled cryostat with a C-type thermocouple spot welded to the back of the crystal to monitor the temperature. The sample can be cooled to 100 K, and heated to 1200 K resistively, or to >2500 K *via* electron bombardment from the back side.

The high temperatures needed to clean and anneal the Re(0001) sample require use of a type C thermocouple, however, the sensitivity ($\Delta V/\Delta K$) to temperatures below 200 K is poor. Commercially available type C vacuum feedthroughs are made using "extension" alloy rather than the actual W-5%Re/W-26%Re thermocouple composition, and our experience was that the temperature readings at low sample temperatures were very sensitive to variations in the feedthrough temperature. Therefore, we fabricated feedthroughs by cementing 1 mm diameter pins made from actual type C material into a commercial feedthrough with two of the pins drilled out, and calibrated the system in the temperature range below 1000 K by attaching an additional type K thermocouple. The type C and type K thermocouples gave temperatures within 1.5 K of each other, and sensitivity to variations in the feedthrough temperature was greatly improved. Nonetheless, we feel that it is prudent to estimate the uncertainty in temperature measurements below 200 K as ±5 K.

Typical sample preparation begins with heating the Re(0001) single crystal to decompose and desorb any adsorbates, including Pt and alumina from previous experiments, as well as annealing the crystal surface. Our procedure, adapted from those developed in the Goodman[63–65] and Madey[66,67] groups, is to heat the sample *via* electron bombardment of the back side, to 1850 K for 4.5 minutes, followed by a flash to 1950 K for 0.5 minutes. XPS and ISS analysis show a surface free of contaminants, save for a sub-monolayer amount of oxygen, and low energy electron diffraction (LEED) analysis by the Goodman and Madey groups showed that the resulting surface is well ordered.

After annealing the crystal and ensuring its cleanliness, the sample is inserted and sealed into an antechamber where the Al_2O_3 thin film is grown. The antechamber (base pressure $\sim 5 \times 10^{-10}$ Torr) allows procedures requiring high pressures to be carried out without affecting the pressure in the main surface analysis chamber. In particular, we find that O_2 exposures in

the main chamber lead to increased water background. The method used here closely follows those developed by the Goodman[63–65] and Madey[66,67] groups, shown to result in epitaxial alumina films with ordered structure as shown by LEED. The Re(0001) substrate is resistively heated to 970 K and 5×10^{-6} Torr of O_2 is leaked into the antechamber, resulting in no measurable change in the main chamber pressure. A resistively heated 99.98% purity alumina crucible filled with aluminum (ESPI Metals, 5N purity), is mounted normal to the Re(0001) surface and brought to the desired temperature for aluminum evaporation. Once the evaporation rate is established, the sample is lowered into position in front of the aluminum source. Growth rates were maintained between 0.2 and 0.3 nm per minute, as determined by XPS analysis of the Al/Re intensity ratio as a function of growth time, and films were grown to thicknesses between 3 and 6 nm. We found that for films in this thickness range, both the electronic structure of the film (*i.e.*, Al and O XPS binding energies), and the catalytic activity and valence band structure of clusters deposited on it, are independent of thickness.[40] In all experiments, XPS was performed after alumina growth both to measure the film thickness, and to verify that the Al and O binding energies and intensity ratios appeared normal for alumina.

For the reactivity experiments, the sample was cooled to ~ 140 K immediately after XPS of the alumina film, then flashed to 650 K to desorb any species (mainly water) that might have adsorbed during the ~ 20 minute cool-down time. As the sample cooled after the flash, deposition of Pt_n was started as soon as the sample reached room temperature (<3 min), continuing until the desired coverage was reached (3–15 min). Deposition was started during cooling in order to minimize the exposure of the cold sample to adventitious adsorbates, as discussed below. The cluster neutralization current was measured continuously during deposition, and used to determine when deposition should be terminated to give consistent Pt coverage. For all the experiments here, the coverage was 1.50×10^{14} Pt atoms per cm^2 (10% of a close-packed Pt mono-layer) deposited in the form of different size Pt_n, at a deposition energy of ~ 1 eV per atom. During deposition the sample was positioned just behind a 2 mm diameter exposure mask, in order to have consistent spot diameters.

To study CO oxidation, the freshly prepared Pt_n/alumina sample was positioned 2.0 mm away from the 2.5 mm diameter orifice in the skimmer cone of our differentially pumped mass spectrometer. The surface was then exposed to 10 L of $^{18}O_2$ at $T_{oxidation}$ of either 300 K or 180 K, and then exposed to 10 L of ^{13}CO at 180 K, before cooling to the 140 K starting temperature for TPR. The 180 K CO dose temperature was chosen to minimize both sticking of CO to the alumina support, and reaction with pre-adsorbed oxygen, and also to allow direct comparison of the results for Pt_n/alumina/Re(0001) with previous studies of Pd_n/TiO_2(110),[6] Pd_n/alumina/Re(0001)[68] and Pd_n/alumina/Ta(110)[40] under these conditions. In some of those systems, CO binding to the oxide support becomes a problematic source of background if the CO dose is done at lower temperatures.

To improve sensitivity for desorbing species, the sample was moved to a position 1.0 mm from the skimmer cone, and then its temperature was ramped at 3 K s^{-1} to 650 K while signals were monitored for the expected $^{13}C^{18}O^{16}O$ product, the unreacted

26444 | *Phys. Chem. Chem. Phys.*, 2014, **16**, 26443–26457

This journal is © the Owner Societies 2014

[13]CO, and for species such as water, unlabeled CO, and CO_2 isotopologs that might form from reaction with adventitious CO or [16]O from the alumina film. This same process (oxidation, CO dose, heat ramp) was carried out two more times to observe the effects of multiple TPRs on the clusters, and then followed by a final CO TPD (no intermediate oxidation step) as a probe of the density of CO binding sites remaining after the series of TPR runs. The final TPD also tests whether any active oxygen remains on the surface at the end of a TPR run. The $T_{oxidation} =$ 300 K and 180 K series of TPR/TPD experiments were done on separately prepared sets of samples, and another fresh set of Pt_n/alumina samples was used for a series of CO TPD experiments to probe the density of CO binding sites on the as-deposited clusters. In those experiments, the same protocol was followed for alumina film growth, cooling, and cluster deposition, but the samples were dosed only with [13]CO (10 L at 180 K) with no oxidation step.

The electronic properties of the as-deposited clusters were probed by a combination of XPS and UPS. To avoid the possibility that adventitious adsorbates or photo-induced damage accumulating during XPS or UPS might affect reactivity studies, the XPS and UPS studies were done on another separate set of Pt_n/alumina samples. In these studies, both XPS and UPS were performed immediately after alumina film growth, and then the samples were cooled to 140 K, flashed to 650 K, and decorated with Pt_n using the same protocol used in the reactivity studies. XPS and UPS were recorded again immediately after deposition to probe the electronic properties of the freshly deposited Pt_n/alumina sample. The small Pt XPS peaks from the clusters are overwhelmed by background from the corresponding Re peaks, which lie just to lower binding energy, however, UPS provides a useful probe of the Pt valence electronic properties. The UP spectra were collected using a homebuilt VUV light source that has been described elsewhere,[69] and the sample was biased to −15.0 volts to improve collection of low kinetic energy electrons for sample work function determination via the high binding energy spectral limit. In the figures below, the binding energy (BE) scale is referenced to the Fermi level (E_F) of the clean rhenium sample, with zero BE taken as the inflection point of the steeply rising rhenium signal. The effects of charging on the Al, O, and Pt spectra appear to be small, as judged by peak widths that are essentially independent of alumina thickness, for the 3–6 nm range used here. Charging effects become obvious for thicker films.

A final set of Pt_n/alumina samples was prepared for ISS studies of cluster morphology, to avoid effects of ISS damage on subsequent spectroscopic or reactivity measurements. Immediately following Pt_n deposition, each sample was probed by a sequence of ISS experiments, consisting of three "low flux" ISS scans, where the He^{+} current on the sample was ~0.1 μA, followed by ten "high flux" ISS scans, with the He^{+} beam set to 1.0 μA. The purpose for the sequence of ISS scans is to detect the presence of, and correct for the effects of any adventitious adsorbates that might be present on the as-deposited samples. We have previously shown[33,38,70] that the He^{+} sputter rate for molecular adsorbates is substantially faster than that for metal atoms in clusters. For this reason, low He^{+} flux is used in the first three scans, so that adsorbate loss can be observed via the increase in signal from newly exposed Pt. Because there is also some loss of Pt by sputtering, the ten high flux measurements are used to establish the Pt sputter rate.

A typical data set is summarized in Fig. S1 of the ESI.† A raw ISS spectrum is given in the inset, and the Pt peak intensity, normalized to the sum of the Al and O signals from the support, is plotted as a function of the cumulative He^{+} exposure during the sequence of 13 ISS scans. The normalization is to compensate for small day-to-day variations in the He^{+} beam conditions. Because sputtering Al or O atoms from the support simply exposes more Al and O atoms, the (Al + O) intensity is found to be quite stable during the sequence of ISS scans. Note that during the initial low flux scans, the normalized Pt signal increased by ~30% due to sputtering of overlying adsorbates, but that with additional He^{+} exposure, the Pt signal begins to decline due to Pt sputtering. The values given below for "as-deposited" Pt normalized intensities (i.e., the Pt/(Al + O) ratios) were obtained by extrapolating this slow decline back to the limit of zero He^{+} exposure.

The initial Pt ISS attenuation is probably mostly due to adsorption of background CO ($\sim 5 \times 10^{-11}$ mbar), which binds strongly to Pt but not to alumina. Adsorption under these conditions can be quite efficient due to substrate-mediated adsorption (reverse spillover), where CO initially impinges on the alumina, then migrates to a stable Pt site during its lifetime on the surface.[33,38,71,72] Fortunately, as discussed below, the adventitious CO is oxidized away during the [18]O_2 exposures, so that no [12]C[16]O[18]O signal is observed in TPR. Similarly, in TPD after a 10 L [13]CO exposure, no [12]CO is observed, suggesting that exchange is reasonably efficient.

It is useful mechanistically, to be able to relate the ion signals observed during TPD and TPR experiments, to the absolute number of the corresponding molecules desorbing from the surface. The following approach was used. With the sample moved away from the mass spectrometer skimmer orifice, various pressures of CO, CO_2, and Ar were leaked into the main chamber via a leak valve that is remote from the mass spectrometer, with pressures measured using two different ionization gauges in the main chamber, corrected using molecular sensitivity factors provided by the manufacturer. Given the 2.5 mm diameter skimmer orifice, it is straightforward to calculate the flux of molecules effusing into the TPD/TPR mass spectrometer, and the ratio of this flux to the corresponding ion count rate gives the overall detection efficiency for the molecules of interest. Because molecules effusing through the orifice should have cosine angular distributions, which are also typical of molecules thermally desorbing from surfaces (unless there is repulsion as the product desorbs along the dissociation coordinate), we need only account for some geometric factors in order to obtain the equivalent detection efficiency for molecules desorbing from the surface. The 2 mm dia. cluster spot is ~40% smaller than the 2.5 mm orifice, and in addition, to avoid any possibility of scratching the single crystal sample, we normally do TPR/TPD with the sample positioned 1 mm from the skimmer orifice. As a result, some molecules desorbing from the cluster spot miss the orifice, and this factor was determined via a few CO TPD measurements made with the positioned nearly touching the orifice (CO does not stick to the alumina, see below). To correct for factors, such as drifting

electron multiplier gain, that might cause day-to-day variations in sensitivity, we perform a simplified version of this calibration every day, using only argon. We estimate that the desorption fluxes determined from this calibration approach should be within a factor of two of the true fluxes.

In order to determine CO desorption energies, the CO desorption spectra were fit to the first order rate equation:[73]

$$I(t) \alpha \frac{-d\theta}{dt} = (\theta(E_{des}) \cdot \nu) e^{\frac{-E_{des}}{kT(t)}}$$

where $I(t)$ is the time dependent CO TPD signal, E_{des} is the desorption energy, ν is the prefactor, $T(t)$ is the temperature as a function of time, and $\theta(E_{des})$ is the occupancy of CO binding sites with different values of E_{des}, *i.e.*, the desired E_{des} distribution. A trial $\theta(E_{des})$ distribution is run through the simulation, the calculated $I(t)$ is compared with the experimental desorption *vs.* time, and then $\theta(E_{des})$ is adjusted until $I(t)$ matches the experiment. Because size-selected cluster samples are time consuming to prepare, and irreversibly changed by a single TPD/TPR run (see below), it is simply not practical to extract ν from a series of coverage-dependent experiments. Therefore, the simulations were done using $\nu = 10^{14}$ s^{-1}, but tested for ν ranging from 10^{13} to 10^{15} s^{-1}, covering a range typically reported for CO TPD.[38] Because the E_{des} distributions shift by only ~7% for an order-of-magnitude variation in ν, we expect that energy scale of the E_{des} distributions should be within ±10% of the correct scale.

Results

Size-dependent CO_2 production

For the $^{18}O_2$ + ^{13}CO reactants used in these experiments, the two main desorption channels are the expected CO oxidation product, $^{13}C^{18}O^{16}O$, and unreacted ^{13}CO. Desorption spectra are shown in Fig. 1 for alumina/Re(0001), and for a typical cluster sample, Pt$_7$/alumina/Re(0001). In both cases, the samples were first exposed to 10 L $^{18}O_2$ at $T_{oxidation}$ = 300 K, and then to 10 L ^{13}CO at 180 K. From the comparison, it is clear that there is no significant adsorption of CO on the alumina film, nor is there any CO_2 production in the absence of Pt clusters. We also looked for desorption of residual $^{18}O_2$, however, none was observed in the temperature range up to 700 K for any of the samples. Signals for both $H_2^{16}O$ and $H_2^{18}O$ were detected during TPR, with integrated intensity less than half that for the CO_2 product. Because this water signal is essentially identical for alumina and Pt$_n$/alumina samples (and independent of Pt$_n$ size), we conclude that most or all results from water adsorbed on the alumina support, which makes up 90% of the surface layer. The only other desorption signal was for $^{13}C^{16}O_2$ (mass 45), and the possible origin of this product isotopolog is discussed below.

The desorption of residual, unreacted ^{13}CO from the Pt$_7$/alumina sample is bimodal, with a relatively small component at ~190 K which will be referred to as the *low temperature* peak, and a larger, broader component peaking at ~520 K which will be referred to as the *high temperature* peak. Because no ^{13}CO desorption is observed from the alumina/Re(0001) sample
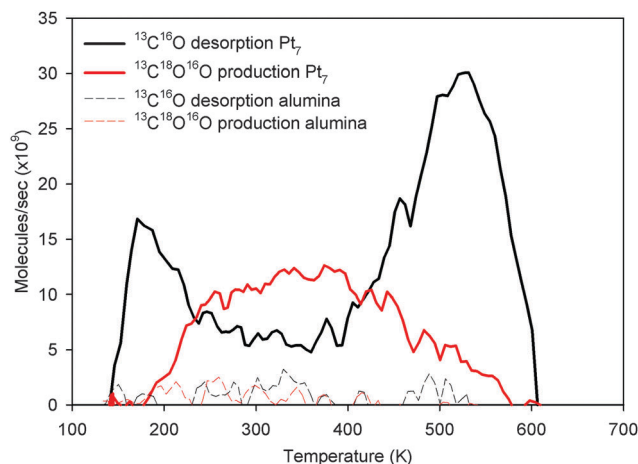

Fig. 1 Residual ^{13}CO (black) desorption and $^{13}C^{18}O^{16}O$ production (red) for the first 300 K oxidation TPR over Pt$_7$/alumina (solid) and bare alumina (dashed). There are two distinct CO desorption peaks at 175 K (low temperature) and 525 K (high temperature), while the CO_2 production is broad and peaks around 350 K between the CO desorption.

under identical conditions, the CO is clearly all bound to sites associated with the Pt clusters. ^{13}CO desorption is observed immediately upon starting the heating ramp at ~140 K, even though the CO dose was delivered at 180 K. This low temperature desorption reflects adsorption of ^{13}CO remaining in the chamber background after termination of the CO dose, as the sample cooled to the 140 K TPR/TPD starting temperature. The integrated exposure during cooling is estimated to have been only ~0.3 L, however, substrate-mediated adsorption results in substantial population in sites with desorption temperature below 180 K. The amount of CO desorbing below 180 K is quite sensitive to small variations in the background ^{13}CO pressure and cool-down time.[40] To avoid any influence of such variations on size-dependent intensity comparisons, only the temperature range above 180 K is included in signal integrations.

CO_2 production is detected over a wide range of temperatures, peaking between 300 and 400 K for all Pt$_n$ – in between the low and high temperature ^{13}CO desorption features. The onset of CO_2 desorption is at ~180 K, *i.e.*, at the CO dose temperature. The absence of CO_2 desorption at lower temperatures is expected, because any adsorbed oxygen capable of reacting with CO at lower temperatures would tend to react away during the CO dose. To test this conclusion, we compared the CO_2 desorption temperature dependence for identical Pt$_7$/alumina/Re(0001) samples, where the CO exposure was done at either 180 K, or 140 K. As expected, in the latter case, CO_2 desorption started at ~140 K. Also, as expected, the magnitude of the low temperature CO desorption peak was substantially larger.

The question, therefore, is how much CO_2 production occurs during the 180 K CO exposure, *i.e.*, how much is missed in the TPR results. Signals for all masses of interest, including $^{13}C^{16}O^{18}O$, are monitored during all reactant exposures. Indeed, $^{13}C^{16}O^{18}O$ signal is observed for Pt$_n$/alumina samples (but not alumina) for roughly the first second of the ~1.5 minute ^{13}CO exposure. Because the $^{13}C^{16}O^{18}O$ signal duration is so short,

it is difficult to estimate the amount, however, it is clear that the $^{13}C^{16}O^{18}O$ production during the CO dose is less than 5% of the amount of $^{13}C^{16}O^{18}O$ that desorbs during the TPR heat ramp.

Fig. 2 shows how desorption of both the unreacted ^{13}CO and the $^{13}C^{18}O^{16}O$ product vary with deposited cluster size. These data are for the first TPR run made after 10 L $^{18}O_2$ exposure at $T_{oxidation}$ = 300 K, followed by 10 L ^{13}CO exposure at 180 K. Fig. S2 (ESI†) gives analogous data for ^{13}CO and $^{13}C^{18}O^{16}O$ desorption in the first TPR run taken on a separately prepared set of samples, where both the $^{18}O_2$ and ^{13}CO exposures were done at 180 K. There are slight differences between the two data sets in the desorption temperature dependences, and in the dependence of intensities on cluster size, but because the two sets of experiments were done on different samples at different times, we do not feel that such small effects are significant. Therefore, to obtain integrated intensities, the $T_{oxidation}$ = 300 K and 180 K data sets have been averaged. The implications of the negligible dependence of CO$_2$ production on $T_{oxidation}$ are discussed below.

Residual ^{13}CO (Fig. 2A) desorbs with a bimodal temperature dependence in all cases, however, the shape and relative intensities of the low and high temperature peaks are size dependent (considering only the T > 180 K range, as discussed above). In particular, samples prepared with Pt_1, Pt_2, and Pt_4 have low temperature peaks which are more intense and persist to higher temperatures than those for the larger clusters, and conversely, the high temperature peak intensities are similar for all the large clusters, but anomalously low for Pt_1 and Pt_2. These differences could reflect size-dependent variations in the distribution of CO binding sites, or size-dependent competition between CO desorption and CO oxidation.

The CO oxidation signal ($^{13}C^{18}O^{16}O$) is, indeed, strongly dependent on cluster size (Fig. 2B). For all sizes, $^{13}C^{18}O^{16}O$ is observed in a broad peak between 180 and 600 K, reaching a maximum at ~350 K, near the minimum between the two CO desorption peaks. The breadth suggests that reaction occurs with a wide range of activation energies, which is not surprising considering that these supported cluster samples presumably have a variety of CO and oxygen binding sites, that site hopping/diffusion may be necessary to bring the reactants together, and that the coverage of one or both reactants varies substantially during the TPR. It is interesting that while the temperature dependence is similar for all cluster sizes, the activity is strongly size dependent.
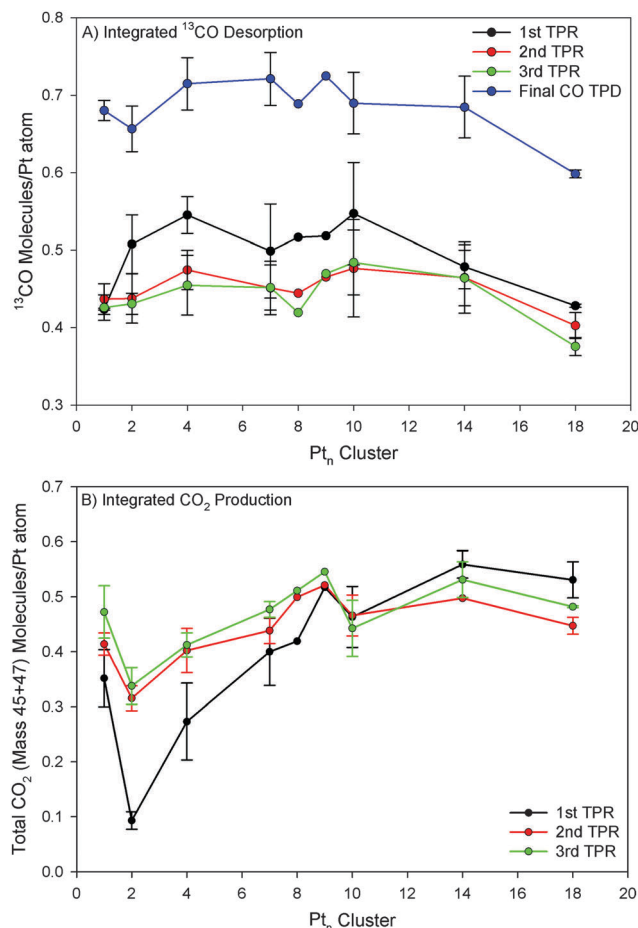
We also monitor signal for other CO$_2$ isotopologs during the $^{18}O_2$ and ^{13}CO exposures, and during the subsequent TPR runs. Weak signal for $^{12}C^{16}O^{18}O$ (mass 46) is observed during the $^{18}O_2$ dose, with similar amounts seen for alumina and Pt_n/alumina samples. Because CO does not stick to alumina in this temperature range (Fig. 1), most of this signal is attributed to reactions of $^{18}O_2$ with CO adsorbed on surfaces such as the oxygen dosing tube and the mass spectrometer differential pumping cone. Because CO$_2$ does not stick on these samples in the temperature range of interest (140 K to 700 K), and no mass 46 is observed during TPR, we conclude that this mass can be ignored in analysis of the results.

On the other hand, the $^{13}C^{16}O^{16}O$ isotopic product (mass 45), is observed to desorb during each TPR, with temperature dependence identical to that for the main product, $^{13}C^{18}O^{16}O$, and with intensity that ranges from 13% to 28% of the total CO$_2$ product intensity. As shown in Fig. S3 (ESI†), the dependence of this mass 45 signal on cluster size is also quite similar to the dependence of the main mass 47 peak, thus this mass 45 signal appears to result from reaction of adsorbed ^{13}CO with ^{16}O on present on the sample surface. The mass 45 signal is larger than would be expected from the measured ^{16}O impurity of the $^{18}O_2$ reactant (~1%), thus there must be another ^{16}O source, such as ^{16}O from the alumina film, or ^{16}O-containing species in the chamber background (*e.g.* H$_2^{16}O$). Regardless of the source, because the cluster size and temperature dependences of the mass 45 desorption are similar to those for the main mass 47 product, we simply add the intensities in calculating the integrated CO$_2$ production. Inclusion of the mass 45 signal has little effect on the relative size dependence.

Fig. 3A shows the integrated residual ^{13}CO desorption as a function of cluster size and Fig. 3B gives analogous results for CO$_2$ production (mass 45 + 47). Because the results for
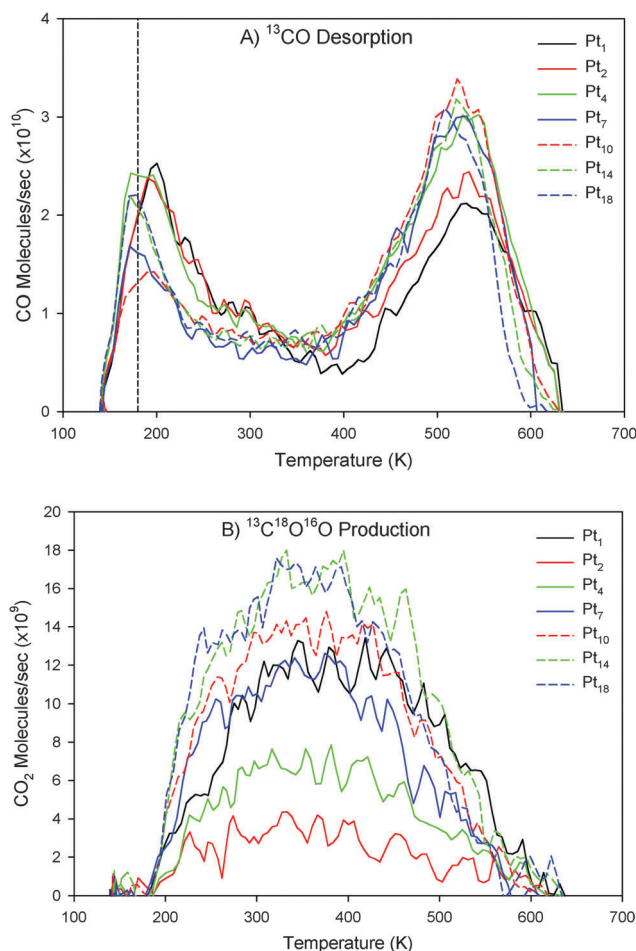
Fig. 2 Residual ^{13}CO (mass 29) desorption from the first 300 K oxidation TPR for all cluster sizes studied (A) and corresponding $^{13}C^{18}O^{16}O$ production (mass 47) (B). The dashed line in (A) indicates the temperature of the CO dose (180 K).

This journal is © the Owner Societies 2014

Phys. Chem. Chem. Phys., 2014, **16**, 26443–26457 | **26447**

Fig. 3 Integrated # of CO molecules desorbed (A) and CO_2 molecules produced (B) during three subsequent TPRs and a final CO TPD. The data represent the average of two different $T_{oxidation}$ with one set for each 300 K and 180 K. The error bars represent the standard error between the two sets. Notice the lack of CO desorption variation with cluster size, where the CO_2 increases by a factor of five between Pt_2 and Pt_{10}. For the final CO TPD, there was no measurable CO_2 production.

$T_{oxidation}$ = 180 K and 300 K are so similar, they have been averaged to generate Fig. 3, but are presented separately in Fig. S4 (ESI†). The error bars in Fig. 3 reflect the differences between the 180 K and 300 K results.

The integrated CO_2 production (Fig. 3B) is strongly dependent on the deposited cluster size with a factor of ~5 increase in CO_2 signal as size increases from 2 to 10, with essentially no further changes for larger clusters. Comparison of Fig. S4b and d (ESI†) suggests that there may be some differences in the cluster size dependence for $T_{oxidation}$ = 180 K and 300 K, but the overall trend is quite similar. The number of CO_2 molecules evolved per Pt atom in the 1st TPR run ranges from 0.1 for Pt_2 to 0.5 for clusters with more than 10 atoms. At least for the larger clusters, the amount of CO_2 produced is comparable to the amount of residual CO, *i.e.*, roughly half the adsorbed CO is converted to CO_2.

Fig. 3 also shows how the chemistry changes in the 2nd and 3rd TPR runs on each sample. Raw data for typical small (Pt_4) and large (Pt_{14}) clusters are shown in the ESI,† Fig. S5. The amount of CO_2 production increases significantly for the smaller

clusters in the 2nd TPR, such that the size dependence is substantially flattened. For the runs with $T_{oxidation}$ = 180 K, the effect is even more dramatic (see ESI,† Fig. S4), with activity for the largest clusters initially higher than in the $T_{oxidation}$ = 300 K runs, decreasing in subsequent runs. There is no significant further change in the 3rd run. In the final TPD of the sequence, without the intervening $^{18}O_2$ exposure, no CO_2 production is observed. (ESI,† Fig. S5).

Desorption of residual CO is not strongly size dependent, although samples with Pt_1, Pt_{14} and Pt_{18} show lower CO desorption, particularly in the 1st TPR. The integrated CO desorption (including only the CO desorbing above 180 K) corresponds to roughly 0.4 to 0.5 CO molecules per Pt atom. The amount desorbing in the 2nd and 3rd TPR runs decreases, particularly for the smaller clusters. Given the increase in CO oxidation activity for the small clusters in the 2nd TPR, a decrease in desorption of unreacted CO is not surprising. In the final TPD, done without the intermediate $^{18}O_2$ exposure, the amount of CO desorbing increases to ~0.7 CO per Pt atom. The increase reflects some combination of the absence of competition from CO oxidation, and the availability of additional CO binding sites when the oxidation step is omitted.

The obvious exception to the trend of increasing activity with increasing deposited cluster size are the samples prepared by deposition of Pt_1, which are significantly more active than the trend would suggest. The CO oxidation activity for Pt_1 is similar to that of samples prepared by deposition of medium size clusters in the Pt_7 size range. This high activity for samples prepared by atomic ion deposition is in contrast to most other systems where we have studied CO oxidation under conditions similar to those used here, where deposited atoms have been found to be completely inactive, or at least less active than any of the larger clusters.[5,6,32,74,75] One obvious way to rationalize the unexpectedly high activity of Pt_1/alumina is to assume that some or all of the deposited atoms agglomerate to form clusters, even for the $T_{oxidation}$ = 180 K experiment, where deposition and reactant exposures were all carried out below room temperature. Enhanced sintering of isolated atoms (compared to pre-formed clusters) has been observed by Buratto *et al.*[76–81] and reflects the fact that for a pre-formed cluster to diffuse, more bonds must be broken simultaneously than are required for diffusion of atoms on a support.

Note however, that there are several pieces of data for Pt_1/alumina that appear to be inconsistent with the idea that deposited atoms all sinter to form clusters. As shown in Fig. 2, the relative intensities of the low and high temperature residual CO desorption features for Pt_1 fit the size-dependent trend just as might be expected if the atoms mostly remained dispersed. In addition, the total amount of CO desorbing in the first TPR (Fig. 3B) is significantly smaller than what might be expected if the Pt were sintered in to clusters with average size around 7 atoms. The anomalous behavior of the Pt_1/alumina samples is discussed further, below.

It is interesting to compare the CO oxidation behavior over Pt_n/alumina/Re(0001) with other systems we have studied under identical conditions, including Pd_n/alumina/Ta(110),[40] Pd_n/alumina/Re(0001),[68] and Pd_n/TiO_2(110).[6] The four systems

26448 | *Phys. Chem. Chem. Phys.*, 2014, **16**, 26443–26457

This journal is © the Owner Societies 2014

are similar in that desorption of unreacted CO has a bimodal temperature dependence, while CO_2 is largely evolved in a broad feature at intermediate temperatures. The CO oxidation activity and dependence on cluster size and $T_{oxidation}$ vary considerably, however. For the Pt_n/alumina/Re(0001) system studied here, between 8% and 50% of the adsorbed CO molecules are oxidized to CO_2, with activity generally increasing with cluster size, with the exception of the samples prepared with Pt_1. For both Pd_n/alumina/Ta(110) and Pd_n/alumina/Re(0001), the cluster size effects are weak but non-monotonic, with oxidation efficiency ranging between 25% and 50%. For Pd_n/TiO$_2$(110), the efficiencies range from 0 to ~10%, with strongly non-monotonic size dependence with local maxima at Pd_2 and Pd_{20}, and Pd_1 being totally unreactive.

For the Pd_n/TiO$_2$ system, the activity and size dependence are strongly dependent on $T_{oxidation}$, with all but Pd_1 active for $T_{oxidation}$ = 400 K, only select sizes active for $T_{oxidation}$ = 300 K, and none active at 200 K.[6] This pattern suggested that there are significant, size-dependent energy barriers for O_2 activation on Pd_n/TiO$_2$. For Pd_n/alumina/Ta(110) system,[40] the CO oxidation activity was significantly lower for $T_{oxidation}$ = 180 K, compared to 400 K, but with weak size dependence. In the present, Pt_n/alumina system, the activities and size dependence are nearly identical for $T_{oxidation}$ = 180 K and 300 K, suggesting that there are no significant energy barriers to O_2 activation.

CO desorption and CO binding sites

As shown in Fig. 3, the integrated amount of unreacted CO desorbing from the samples in TPR is large, and weakly correlated with cluster size, unlike CO oxidation activity, which is strongly size-dependent. Furthermore, while CO_2 production increases by a factor of up to 3.5 for the smaller clusters in the 2nd and 3rd TPR, the residual CO intensity decreases by only 10–15%. These trends suggest that CO is not the limiting reactant that determines the efficiency of CO oxidation.

As Fig. S5 (ESI†) shows, the temperature dependence of the residual CO desorption changes during the sequence of TPR/TPD runs. The high temperature CO desorption feature decreases by ~15–20%, mostly between the 1st and 2nd TPR run, while the low temperature feature remains roughly constant. In the final CO TPD, without intervening O_2 exposure, there is a large increase in CO desorption (Fig. 3A), and Fig. S5 (ESI†) shows that this increase results primarily from an increase in CO desorption at intermediate to high temperatures.

For comparison to the TPR results, we also measured CO TPD from a separately prepared set of samples that were exposed to CO at 180 K and heated at 3 K s^{-1}, but without any O_2 exposure. Fig. 4A shows CO desorption observed in the first TPD run on freshly prepared samples, and can be compared to the residual CO desorption observed in the first TPR run (Fig. 2A – note different vertical scales). Fig. 4B shows the desorption observed in a second TPD run, also with CO exposure at 180 K.

Several points are obvious. Considerably more CO desorbs in TPD than TPR, reflecting the absence of competition between CO desorption and CO oxidation, as well as the absence of pre-adsorbed oxygen which might block CO binding sites.
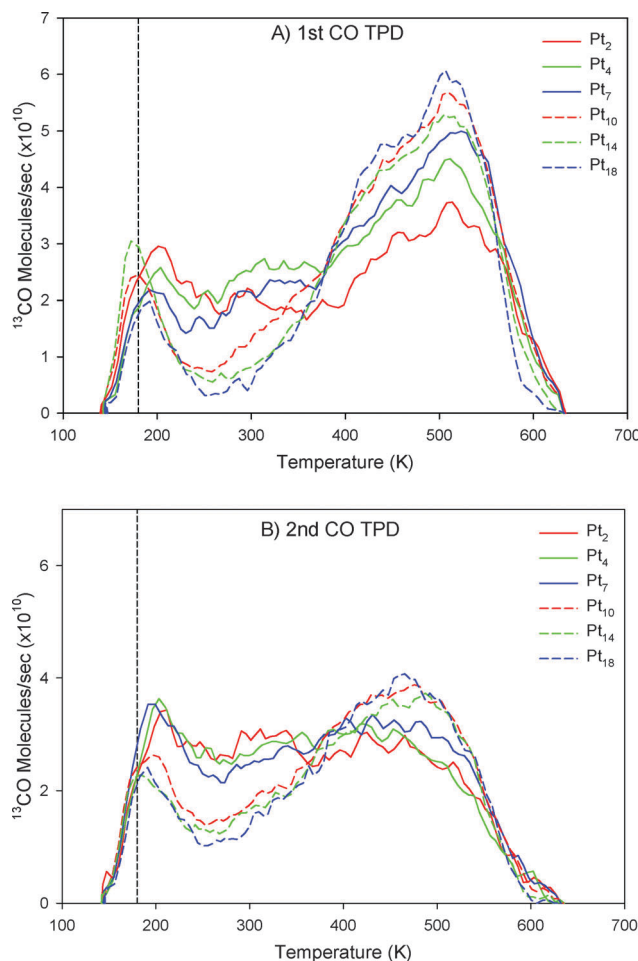

Fig. 4 Integrated ^{13}CO (mass 29) desorbing from the unoxidized surface after 10 L ^{13}CO exposure at 180 K as a function of cluster size for the first CO TPD (A) and second CO TPD on the same surface (B). Notice the distinct drop in the size of the high temperature CO peak between the first and second CO TPD. The dashed line in both graphs indicates the CO dose temperature (180 K).

There is relatively little difference in the low temperature CO desorption, but the high temperature desorption feature is much more intense, especially for the larger cluster sizes, where the competition from CO oxidation is strongest. Furthermore, in TPR, there is a pronounced minimum around 350 K, with fewer than 10^{10} CO per s desorbing. In TPD, the large clusters still show a minimum below 10^{10} CO per s, but at ~100 K lower temperature. The Pt_2, Pt_4, and Pt_7 show much weaker minima, with evidence for a third desorption feature peaking around 300 K. In the 2nd CO TPD, the intensity of the high temperature CO desorption feature decreases substantially, particularly for the larger clusters. In contrast, the desorption intensity below 350 K increases slightly, particularly for the large clusters. A third CO TPD run was also done, resulting in no significant changes compared to the 2nd TPD run.

The CO desorption temperature dependences were fit, as discussed above, to extract the corresponding distributions of desorption energy (E_{des}). Two examples are shown in Fig. 5, for CO TPD from Pt_4 and Pt_{14}, representing typical small and

large clusters. The figure shows the raw experimental data as points, and the simulations as curves. Note that there are small fluctuations in both the data and simulations, notably around 250 K for the Pt$_4$ example. These resulted from small fluctuations in the sample heating rate, causing fluctuations in the desorption signal. The simulations capture this behavior because they were done using the measured temperature *vs.* time data. The resulting $\theta(E_{des})$ distributions are also shown. Because there are clearly three desorption features for the small clusters, all the fits were done assuming the existence of low, mid, and high E_{des} components, each parameterized consistently for all cluster sizes.

For Pt$_4$, representative of the small clusters, all three components are significant, and the low, mid, and high E_{des} components peak at roughly 0.5 eV, 0.9 eV, and 1.6 eV, respectively. The fact that the low E_{des} component peaks at 0.5 eV simply reflects the fact that the CO exposure was done at 180 K ($E_{des} \approx 0.55$ eV) such that more weakly bound sites were only populated by background CO as the sample cooled to 140 K. This component would have been larger, and peaked at lower E_{des}, if the CO exposure had been done at lower temperatures.

For Pt$_{14}$, representative of the larger clusters, the CO desorption shows a pronounced minimum between 250 and 300 K, and the temperature dependence could have been fit without a mid-E_{des} fit component. For consistency, a mid-E_{des} component was included for all cluster sizes, but obviously this component is small for the large clusters.

The results of the fits are summarized in Fig. 6, which shows the integrated intensities of the three CO desorption components as a function of cluster size, for the first and second TPR (top frame) and TPD (bottom frame) experiments. The results are plotted as the number of CO molecules desorbing per Pt atom. One obvious point is that the intensity of the high temperature desorption component is much higher in the first TPD (~ 0.45–0.8) than in the first TPR (~ 0.2–0.35). In both cases, the intensity increases with cluster size to about 10 atoms, and then is constant (TPD) or decreases (TPR) with further increase in cluster size. The mid-temperature component is small (~ 0.07) for all cluster sizes in TPR, while in TPD, this component is sizable (~ 0.2) for small clusters, falling to essentially zero with increasing cluster size. The low-temperature component is small (~ 0.1) in both TPD and TPR and decreases with increasing cluster size.

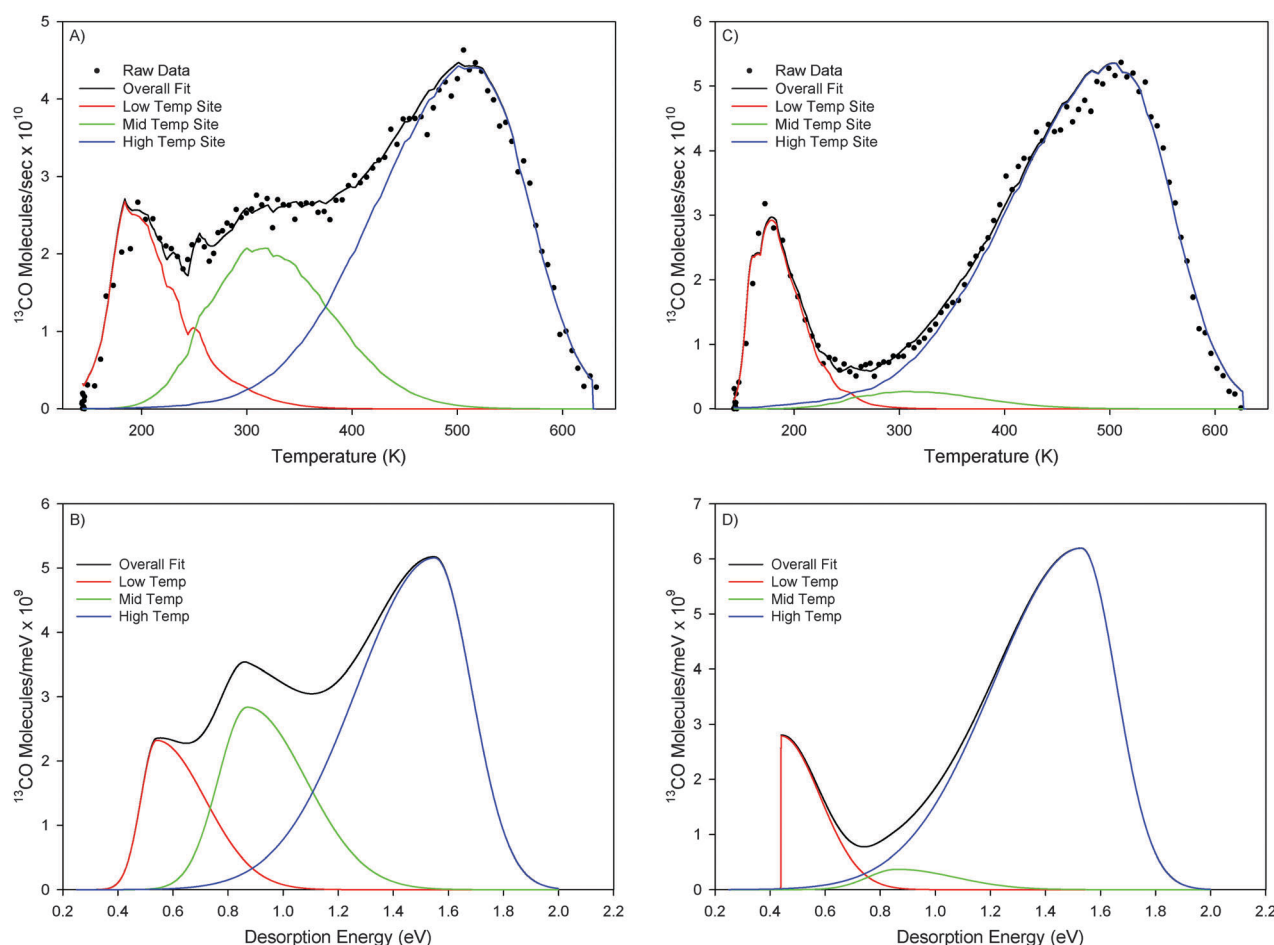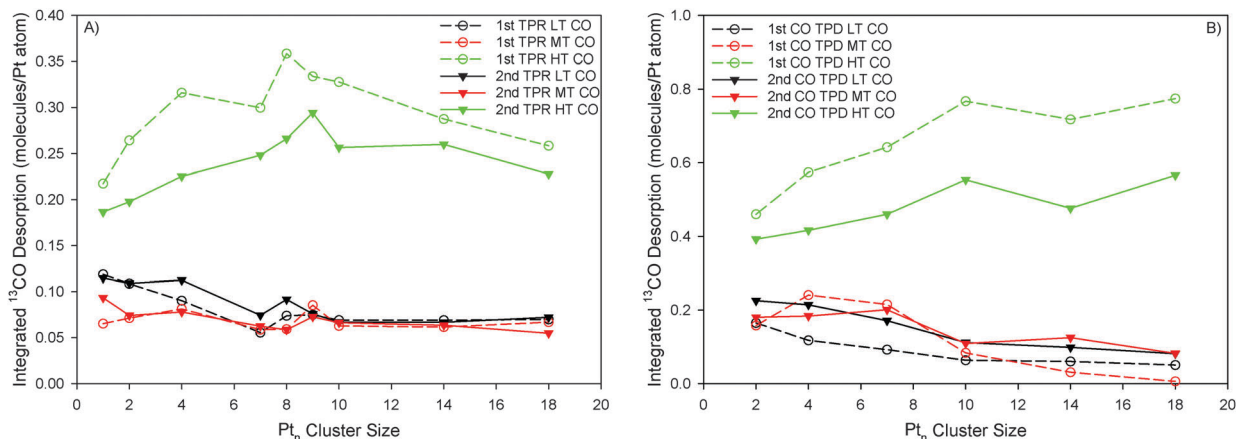**Fig. 5** CO desorbing during the 1st CO TPD for Pt$_4$ and Pt$_{14}$ and their fits (A,C) along with the accompanying energy of desorption (E_{des}) fits (B,D). The main difference between the two cluster sizes is a larger mid-temperature feature and smaller high-temperature feature for the smaller cluster (Pt$_4$) as opposed to the larger cluster (Pt$_{14}$).

Fig. 6 Intensities for low temperature (LT − black), mid-temperature (MT − red), and high temperature (HT − green) residual CO desorbing during the first (dashed) and second (solid) 300 K oxidation reactions (A). Notice the significant decrease in the HT CO desorbing during the second run, as compared to very little change for the LT and MT CO peaks. The same LT, MT, and HT desorbing CO is shown in (B) for two consecutive CO TPDs. Again, the HT CO peak significantly reduces in the second CO TPD; however, now the LT peak appears to increase slightly for all cluster sizes, while the MT peak increases for the large clusters only.

In both TPD and TPR, the intensity of the high temperature feature decreases by ~30% in the second run, indicating significant loss of the most stable CO binding sites due to changes in the samples. In TPR, the low and mid-temperature features show essentially no change in intensities between the 1st and 2nd runs, while in TPD, the low temperature feature decreases by ~40% in the 2nd run. The mid-temperature feature, which was significant only for the small clusters in the first TPD, shows little change for the small clusters, but increases significantly for the large clusters in the 2nd TPD run. In essence, the temperature dependence of CO desorption in TPD flattens out significantly in the 2nd TPD (Fig. 4B).

Valence band measurement with UPS

In order to investigate the electronic structure of the model catalysts, X-ray and ultraviolet photoelectron spectroscopies (XPS/UPS) were employed. The XPS peaks from 0.1 ML Pt are weak, and in this system they are unusable due to high background from the analogous Re 4f XPS features, which lie just to lower binding energy. XPS was used to characterize the alumina film, *via* the Al 2s and O 1s peaks, which did not show any significant changes as a function of deposited Pt_n size. The focus here is on UPS measurements relating to the electronic structure of the Pt_n/alumina samples, because previous work suggests that we might expect a size-dependent correlation between electron binding energies and activity.[6,39,40,82]

Fig. 7 shows the UP spectra for alumina/Re(0001) and Pt_7/alumina/Re(0001), focusing on the energy range near the Fermi level (E_F), corresponding to the band gap of the alumina film. The energies are referenced to E_F of the Re(0001) support which, as expected, is insensitive to growth of the alumina film, deposition of Pt, *etc.* The sharp rise that goes off scale at higher binding energies is the valence band from the alumina film, which reaches a maximum intensity of ~175 000 counts per second at ~7.0 eV. For the alumina sample, there is smooth, weak signal in 0 to 4 eV range attributed to a combination of

photoelectrons from the Re support that survive passage through the ~4 nm alumina film, along with signal from mid-gap states due to defects or impurities in the alumina film. Our main interest here is in the UPS signal arising from the deposited Pt clusters, which is easily obtained by subtracting the spectra measured before and after Pt_n deposition.

The inset to Fig. 7 shows the subtracted Pt_7 spectrum. To approximately correct for experimental broadening, we adopted the procedure suggested by Parkinson and Schlaf,[83,84] where the raw spectrum is fit to a Gaussian-convoluted step function, and then a line tangent to the inflection point in the fit is extrapolated to baseline to give an estimate for the onset energy of the Pt valence band.

Fig. 8 compares the onset energies of the Pt valence bands, referenced to E_F, with the CO_2 production in the first TPR run.
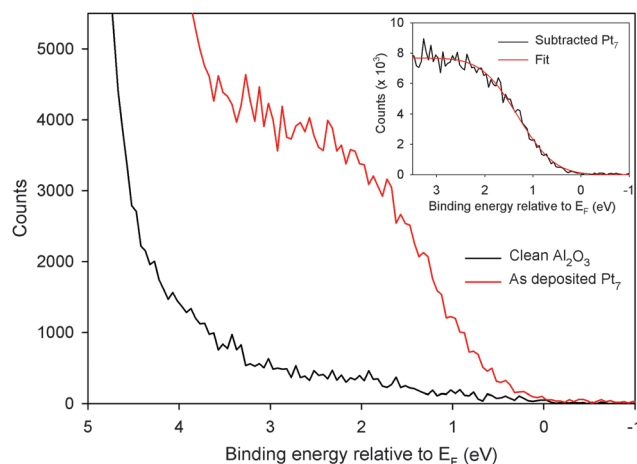
Fig. 7 Raw UP spectra near the Fermi level for a 4.2 nm alumina film (black) and the same film with 10% ML of Pt_7 deposited (red). The sharp rise in the spectrum at >4 eV is the onset of the O 2p band. The inset shows the Pt_7 spectrum with the clean alumina spectrum subtracted out (black) along with a fit (red) to determine the onset of the Pt_7 valence band.
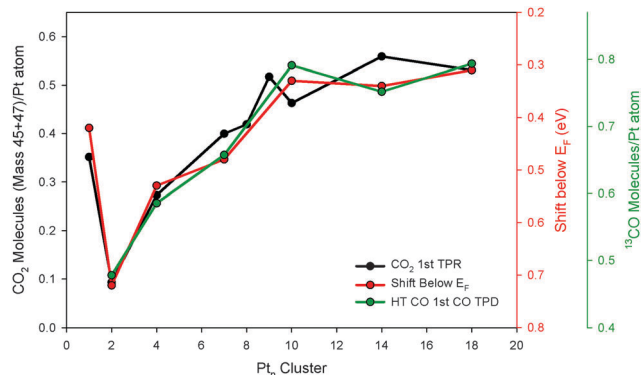
This journal is © the Owner Societies 2014

Phys. Chem. Chem. Phys., 2014, **16**, 26443–26457 | **26451**

Fig. 8 There is a strong correlation between CO_2 production (T_{ox} = 300 K, black line), the shift of the valence band below the Fermi level (red), and the amount of CO desorbing from the high temperature (HT) binding site during the 1st CO TPD on a fresh sample (green). Note the inverse scale for the valence band shift below the Fermi level.

Fig. 9 As deposited Pt/(Al + O) ISS values as a function of cluster size. The ~15% drop in intensity between Pt_7 and Pt_8 suggests some distribution of clusters on the surface are becoming 3-dimensinal or multilayer, and remaining as such through Pt_{14}, where there is another drop to Pt_{18}.

Note that the Pt valence band onset energy is plotted on an inverted scale, *i.e.*, the CO oxidation activity and Pt valence band onset energy appear to be strongly anticorrelated. For the small clusters, the onset energy is large, and activity is low. As density of states near E_F grows with increasing cluster size, the activity increases, but then for Pt_n, $n \geq 9$, the onset energy becomes constant at just over 0.3 eV, and the activity levels off. The onset energy for samples prepared by Pt_1 deposition is anomalously low, similar to what might be expected for a sample with clusters in the 7–9 atom size range.

The figure also plots the integrated intensity of the high temperature CO desorption feature measured in CO TPD (from unoxidized Pt_n/alumina/Re(0001)), taken from the fits described above. The intensity of this component of CO desorption in TPD appears to be correlated with CO_2 production activity in TPR. Comparison with Fig. 6 shows that the low or mid-temperature desorption intensities in TPD are not obviously correlated with activity, and the same is true for the high temperature CO desorption measured in TPR. The implications are discussed below.

Cluster morphology from as-deposited ISS

The UPS results show that there is a correlation between Pt electronic structure and activity, but it is also useful to consider possible correlations with cluster morphology. Using the method described above, a separate set of samples was probed by low energy He$^+$ ion scattering (ISS), and the as-deposited Pt ISS signal is plotted as a function of cluster size in Fig. 9. The Pt signal is normalized to the sum of Al and O signals in order to correct for any day-to-day variations in the He$^+$ beam intensity. Because each data point requires a fresh sample, and the samples cannot be used in subsequent reactivity or spectroscopy experiments due to He$^+$ impact damage, it was not practical to repeat the entire set of measurements. The most interesting effect is the sharp drop between Pt_7 and Pt_8, and for those two sizes, we ran three sets of measurements each, all on freshly prepared samples, and the error bars reflect the standard errors of the repeated runs.
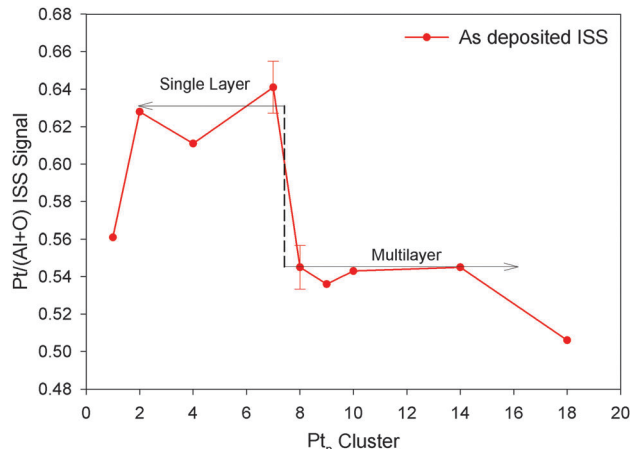
The peaks in ISS (Fig. S1, ESI†) arise from single scattering events, mostly involving atoms in the top-most layer of the sample.[38,71,72,85–87] Because the samples all contain the same total number of Pt atoms, intensity variations with cluster size provide insight into morphology. If the clusters deposit as single layer thick islands, then all the Pt is in the top layer, resulting in maximum Pt ISS intensity. If, however, the clusters deposit as multilayer structures, where some fraction of the Pt is not in the top layer, then the Pt ISS intensity should be reduced by a comparable fraction.

The results in Fig. 9 suggest that the samples fall into three groups. Samples prepared with small clusters (Pt_n, n = 2, 4, 7) all have similar Pt intensities in the range from 0.61 to 0.64. There is an abrupt 15% drop in Pt ISS intensity between Pt_7 and Pt_8, and then the mid-size clusters (Pt_8–Pt_{14}) all have intensities near 0.54. Finally, for Pt_{18}, there is a further drop to ~0.5. Once again, the sample prepared by Pt_1 deposition is an outlier, with Pt ISS intensity that is similar to values observed for the mid-size clusters (Pt_8–Pt_{14}), providing further evidence that deposited Pt atoms are sintering to produce clusters. The ISS results also further support the conclusion that sintering is not extensive for deposited clusters, even as small as Pt_2. As a result, sample morphology, CO oxidation activity, CO binding properties, and electronic structure all retain strong dependence on deposited cluster size.

The ISS data indicate that Pt_2–Pt_7 have a similar large fraction of the Pt atoms in the surface layer, and if we assume they are not sintered significantly, then the obvious interpretation would be that the small cluster form single layer structures on the surface, where all Pt atoms are exposed. The intensity drop into the Pt_8–Pt_{14} size range indicates that these clusters begin to have one or two atoms in a second layer, on average, and the further intensity decrease for Pt_{18} indicates that the trend toward 3D cluster structures continues with increasing size. To the extent that there is some sintering of even the smallest clusters, the stepwise decrease in Pt ISS intensity with

26452 | *Phys. Chem. Chem. Phys.*, 2014, **16**, 26443–26457

This journal is © the Owner Societies 2014

increasing size would still imply a stepwise transition to increasingly 3D structures. Similar transitions from single layer to multilayer geometries are seen for Ni_n/TiO_2(110),[88] Au_n/TiO_2(110),[5] Ir_n/TiO_2(110),[71] Pd_n/TiO_2(110),[6,38] and Pd_n/alumina/Re(0001).[89]

Discussion

The origin of correlations between activity, valence band energy, and CO binding

One striking result of this study is the correlation between CO_2 production, the Pt valence band onset energy, and the amount of CO desorbing in the high temperature feature in TPD. It is not surprising that the Pt electronic structure should influence chemistry on the clusters, but such a strong one-to-one anti-correlation suggests that electronic structure is the dominant factor controlling activity. Other factors that might be expected to influence activity include cluster morphology and the availability of different types of reactant binding sites.

The ISS results suggest that morphology correlates with CO oxidation activity only in the general sense that activity increases over the same size range where a transition to more 3D geometries occurs. On the other hand, the size dependence of activity and Pt ISS differ substantially in detail, with smooth growth in activity with size, contrasting with step-wise decreases in the fraction of Pt in the surface layer. This is not to say that there are not structural effects on activity, but only that activity does not correlate with the qualitative morphology changes detectable by ISS.

The availability of binding sites associated with the Pt clusters was probed *via* TPD (no CO adsorbs on the alumina film in the experimental temperature range). As shown in Fig. 8, the intensity of the high temperature CO TPD feature correlates well with CO oxidation activity. Note, however, that the variation in activity with size is about three times stronger than the variation in the number of high temperature CO binding sites. The interpretation of this correlation depends on whether oxygen or CO is the limiting reactant under our conditions. If CO were limiting, then the correlation might suggest that CO molecules bound in the most stable binding sites are particularly reactive with co-adsorbed oxygen. In that case, activity might be expected to scale with the number of such sites, but it is not clear why the most stable CO should be most likely to react, or why the activity should vary three times more strongly with size than the site density. As discussed below, however, it appears that oxygen is the limiting reactant under our conditions, and in that case, the obvious interpretation of the correlation is that the same type of binding sites are responsible for O_2 adsorption and for the high temperature CO desorption component in TPD.

It might seem surprising that oxygen could be the limiting reactant, given that in our TPR protocol, the samples were exposed to O_2 before CO. If O_2 adsorption were efficient, the 10 L O_2 exposure used (~ 2 O_2 incident per surface atom) would cover the Pt clusters with oxygen; however, several observations suggest that oxygen adsorption is inefficient. The fraction of CO adsorbed during TPR that is converted to CO_2 varies

from $\sim 10\%$ for Pt_2 to $\sim 50\%$ for $Pt_{\geq 9}$, *i.e.*, 50%–90% of the CO desorbs unreacted. Furthermore, there does not appear to be any active oxygen remaining on the samples after the CO has desorbed, as shown by the absence of CO_2 production during the final CO TPD run carried out after the series of TPR runs.

Further evidence that O_2 adsorption is inefficient on these samples comes from the observation that pre-exposure to O_2 does not substantially interfere with subsequent CO adsorption, at least for the larger clusters. As shown in Fig. 6B for CO TPD from unoxidized samples, the contributions of the three CO desorption components vary with cluster size, however the total CO desorption is roughly one CO molecule per Pt atom for all samples. In TPR from oxidized samples, the CO and CO_2 signals (Fig. 3A and B) also add up to about one molecule per Pt atom for Pt_n, $n \geq 7$, indicating that O_2 exposure did not significantly reduce the number of sites for subsequent CO adsorption. Most work in the literature on Pt or Pd single crystals tends to suggest that surface oxidation does block subsequent CO adsorption. For example, experiments by Yates *et al.*[90–92] on the Pt(355) and (112) stepped surfaces showed that oxygen prefers to bind at steps sites, and then blocks CO from binding at those sites. We do not know how oxygen and CO co-adsorb on these small Pt clusters, however, it seems likely that if the oxygen coverage were high, it would block sites for subsequent CO adsorption.

ISS also provides some insight into binding of oxygen and CO. Exposure of Pt_n/alumina samples to 10 L of CO resulted in >80% attenuation of the Pt ISS signal, indicating that the clusters were largely covered by CO, which attenuated scattering from underlying Pt by a combination of shadowing, blocking, and reduction in He$^+$ ion survival probability (ISP).[33,38] In contrast, a 10 L O_2 exposure resulted in only $\sim 25\%$ attenuation of Pt ISS signal, suggesting that most of the cluster surface remained free of adsorbed oxygen. In both cases, the relationship between coverage and attenuation depends on the nature of the binding sites. In our experimental geometry, CO or O atoms bound in atop sites would completely block scattering from the underlying Pt atoms, and might cause additional attenuation by shadowing or reducing the ISP for scattering from other Pt atoms. Binding in bridging or hollow sites on the cluster surfaces would not cause blocking, but would still result in attenuation by shadowing and reduction in the ISP. Binding to sites at the cluster periphery would have minimal effect on Pt ISS signal. The amounts of CO and CO_2 desorbing during TPR imply the CO coverage at the start of the 1st TPR run was roughly one CO per Pt atom, independent of cluster size, which is consistent with the near complete attenuation of Pt ISS signal. The amount of CO_2 produced implies that there must have been at least 0.1 to 0.5 active O atoms per Pt atom, with the coverage increasing with cluster size. On the other hand, the small effect of O_2 exposure on ISS suggests that the oxygen coverage on Pt probably isn't much higher than this lower limit, *i.e.*, O_2 adsorption is relatively inefficient (≤ 0.5 O atoms/Pt from a dose corresponding to 2O_2 incident per atom).

The question is what limits O_2 binding and activation. The similarity in CO_2 production for O_2 exposures at 180 and 300 K

This journal is © the Owner Societies 2014

Phys. Chem. Chem. Phys., 2014, **16**, 26443–26457 | **26453**

suggests that the limiting factor is probably not energetics, at least in this temperature range. The other obvious limiting factor would be the availability of suitable binding sites. The correlation of CO oxidation activity with the density of the most stable CO binding sites tends to support this idea, and suggests that O_2 adsorption requires the same type of sites that support the strongest CO binding.

The idea that O_2 activation requires sites similar to those responsible for the most stable CO binding, might also explain why CO oxidation activity varies three times more strongly with size than the density of such sites. Suppose that O_2 binding and activation involves dissociation and binding of O atoms into adjacent sites on the clusters. For Pt_n, $n \geq 9$, the number of such sites per Pt atom is roughly constant at ~ 0.8 (Fig. 8), *i.e.*, there are ~ 6 to 12 sites per cluster, allowing relatively efficient oxygen adsorption. Because the samples have constant Pt coverage, the increase in number of sites per cluster is offset by the decrease in number of clusters, leading to size-independent CO oxidation activity. For smaller clusters, the number of sites per cluster becomes small. For example, the number of high temperature CO sites per Pt_4 is only ~ 2.4 on average, and one might expect that O_2 dissociative adsorption would be efficient only for a narrow range of interaction geometries. On average, the samples prepared with Pt_2 support binding of only one CO molecule per cluster in the high temperature site. In that case, we might expect that isolated Pt_2 clusters would be unable to bind O_2 at all, and therefore would be inactive. The small activity observed for samples with Pt_2 could be explained by the fact that for 0.1 ML coverage of such small clusters, the average center-to-center cluster separation is only ~ 1.2 nm, thus there is a significant probability for accidental overlaps of cluster landing positions, which would form Pt_4, or larger clusters, able to support O_2 dissociative adsorption. With increasing cluster size, the center-to-center cluster spacing becomes larger (*e.g.* 2.6 nm for Pt_{10}), making overlapping deposition less likely.

Fig. 8 shows that CO oxidation activity is also anticorrelated with the onset energy of the Pt valence band, relative to the Fermi level (E_F) of the samples. We have previously shown similar anticorrelations between activity and metal cluster core level energies,[6,19,40] but here we are looking at the valence band, which one might expect to be more directly related to activity. Norskov and co-workers, using DFT calculations, first pointed out that for many catalytic metals, there is a correlation between the energy of the center of the d band, relative to E_F, and binding energies for oxygen and other adsorbates.[93,94] The correlation is explained in terms of filling of bonding and antibonding orbitals formed by overlap of adsorbate orbitals with the metal d-band. We are not able to measure the Pt d-band center because the lower end of the d-band overlaps with the alumina film valence band. What we can measure is the filled Pt density of states in the range between E_F and the onset of the alumina band, and in particular, the onset energy, *i.e.*, the highest occupied level.

The onset energies are ~ 0.3 eV below E_F for Pt_{10}–Pt_{18}, then rapidly increase with decreasing size to >0.7 eV for Pt_2, and this increase in valence band onset energy correlates with a steep decrease in activity for CO oxidation. The anomalous behavior

of samples prepared with Pt_1 will be discussed below. It is not surprising that activity should decrease with increasing binding energy of the Pt valence electrons, because one might expect that O_2 activation is facilitated by electron transfer from Pt into the O_2 antibonding π^* orbital. The binding energy measured by UPS is, however, influenced by both the initial and final states of the photoemission process. The final state for ionization out of an orbital localized on a Pt cluster is a positively charged cluster, and the final state energy should decrease with increasing cluster size due to greater charge delocalization. Some of the increase in Pt valence binding energy for the small Pt clusters is, therefore, expected to result from greater final state charge localization. Note, however, that if the O_2 binding and activation process also requires electron transfer from Pt to O_2, the transition state energy for that process must also be affected by greater charge localization in small clusters.

It is interesting to compare these UPS results, and their correlation with activity, with results from Watanabe and coworkers, who used XPS to examine $Pt_n/TiO_2(110)$ (n = 4, 7–10, 15). They observed that the Pt 4f core level binding energy decreases with increasing cluster size, then becomes nearly constant for $n \geq 8$. STM showed that the cluster structure changed from single layer to multilayer at the same size,[16,19] and the activity for CO oxidation also leveled off for $n \geq 8$. Computational work by Dai and coworkers also saw Pt_8 deviate from typical single layer trends seen for Pt_4–Pt_7 with Pt_8 looking more strongly multilayer.[25] For Pt/TiO_2, the morphology and electronic structural transitions both occur at Pt_8, making it difficult to tell whether one or both are responsible for the leveling off in activity. For Pt_n/alumina studied here, the transition to multilayer geometries also occurs at Pt_8, however, the leveling off of the valence band onset energy occurs at $\sim Pt_{10}$. Since this is also where activity levels off, it appears that electronic effects are more important in determining activity in this system.

The Pt_n/alumina results can also be compared to what is seen under very similar conditions for Pd_n on several different supports. In the $Pd_n/TiO_2(110)$ system,[6,36] there are cluster size-dependent activation energies associated with O_2 adsorption and activation, which clearly control the efficiency of CO oxidation, which varies by a factor of ~ 8 with cluster size for 400 K oxidation temperature. Activity was found to be strongly anti-correlated with the Pd 3d core level binding energy, as measured by XPS. For Pd_n/alumina/Ta(110),[40] CO_2 production was weakly dependent on oxidation temperature, and for Pd_n/alumina/Re(0001),[68] *i.e.*, the support used here, there was essentially no effect on CO_2 production in TPR from oxidizing at 180 K *vs.* 400 K, or from increasing to a 50 L O_2 exposure. CO oxidation efficiency was high ($\sim 50\%$), and weakly dependent ($\pm 15\%$) on cluster size. There was some evidence of anticorrelation between activity and the Pd 3d binding energy, however, the weak dependence of both observables on cluster size limited the usefulness from a mechanistic perspective. Here, there is also little dependence of CO_2 production on oxidation temperature, but activity does vary by more than a factor of five with size, and there is a clear anticorrelation with Pt valence onset energy and a correlation with the amount of CO desorbing at high temperatures.

26454 | *Phys. Chem. Chem. Phys.*, 2014, **16**, 26443–26457

This journal is © the Owner Societies 2014

While the main motivation of this paper is on the inherent size-effects of the physical and chemical properties of these Pt_n model catalysts, from a practical perspective it is interesting to assess the stability of the catalysts. For this reason, a series of TPR experiments were sequentially performed to examine the effects of heating and reaction on catalytic activity and the physical and electronic properties. It is apparent that there are significant changes to the catalyst activity after the first cycle (Fig. 3 and Fig. S5, ESI†) with a "stable" state persisting for the following two cycles. It is, however, unclear what changes are occurring, which is why our discussion focuses on the catalytic activity and properties of the surface for the first reaction cycle. That being said, possible explanations for the changes to the catalyst behavior and properties are discussed briefly below.

Sintering and the anomalous behavior of Pt_1/alumina

As shown in Fig. 3, the activity of samples prepared with small Pt_n ($n \leq 8$) is low in the first TPR experiment, but increases substantially in the 2nd TPR, such that the cluster size dependence of activity is substantially weakened. There is little further change in the 3rd TPR. Both the amount of CO desorbing unreacted (Fig. 3) and its dependence on temperature (ESI,† Fig. S5) also change substantially in the 2nd TPR. Similarly, in CO TPD from samples never dosed with O_2, the amount and temperature dependence of CO desorption changes between the 1st and 2nd TPD run (Fig. 4). The obvious interpretation of these changes is that the small clusters undergo a sintering or ripening process under these conditions, which increases the average size of the clusters. The increase in activity, for example, would be consistent with Pt_2 or Pt_4 having agglomerated into clusters with average size of roughly 4 or 8 atoms, respectively, in the second TPR. Examination of the CO TPD results in Fig. 4, however, shows that the situation is more complicated. If the only changes were a doubling, on average, of the deposited cluster size, then we would expect that the high temperature CO desorption feature in the 2nd CO TPD would be increase significantly for the samples prepared with Pt_2 or Pt_4, however, this CO desorption feature decreases substantially for all samples in the 2nd TPD. Evidently there are additional changes, possibly to cluster morphology or to the alumina support, that occur during TPR or TPD.

A related observation is that samples prepared by deposition of Pt_1 show activity and other properties that are quite different from those expected from the size-dependent trends. For example, the activity in the first TPR for Pt_1/alumina is roughly what might be expected for Pt_6, and the Pt ISS signal (Fig. 9) is similar to what might be expected if the average cluster size were in the 8–14 atom range. On the other hand, the temperature dependence of the CO desorption in TPR (Fig. 2A) is not at all what would be expected from a distribution of larger clusters.

These apparently contradictory observations for Pt_1 can be rationalized as follows. Suppose that $\sim 60\%$ of deposited atoms diffuse and sinter into large clusters, but that the other 40% remain dispersed, perhaps stabilized by binding at defects in the alumina support. If, as discussed above, O_2 binding and activation requires at least a pair of suitable O atom binding sites, then the dispersed atoms would be completely unreactive,

and the samples would show activity corresponding to 60% of the large cluster activity, as is observed. If the dispersed atoms also have low CO binding energies, then this would also explain why the high temperature CO desorption peak is relatively weak for the Pt_1 sample. The low as-deposited ISS signal could also be explained if the sintered clusters were large enough to have multilayer structures.

For sintering to account for the anomalous behavior of Pt_1, we would need to assume that deposited Pt atoms diffuse and sinter more readily than pre-formed clusters, unless they trap at defects. Campbell and co-workers[95,96] have showed that as nanoparticles become smaller, their chemical potential increases, causing them to more readily sinter. Enhanced diffusion and sintering of isolated atoms has been observed directly with STM by Buratto and co-workers,[76–81] with TEM by Datye and co-workers,[97] and computationally by Alexandrova and co-workers.[98] The anomalously high sintering propensity for deposited atoms, compared to pre-formed clusters, reflects the fact that site hopping of free atoms requires breaking fewer bonds simultaneously compared to diffusion or breakup of pre-formed clusters, resulting in lower activation barriers. In this system, it appears that atoms are mobile during the below-room-temperature deposition, but deposited cluster remain mostly intact. During TPD/TPR, the clusters also sinter, presumably due to the combination of higher temperatures and adsorbate binding.

Conclusion

We have shown that for the Pt_n/alumina model catalyst system, there is a strong cluster size dependence for CO oxidation, where the amount of CO_2 produced varies with cluster size by a factor of about five for the first TPR. Following the first reaction cycle, much of this size dependence is washed out resulting in a final state reactivity that is high, stable, and no longer very size dependent. Probing the CO binding sites shows a correlation between CO oxidation activity and density of the most stable CO binding sites, suggesting that these sites are also responsible for oxygen adsorption and activation. CO oxidation activity is also anticorrelated with size-dependent shifts in the Pt_n valence band onset energies, but not correlated in detail with changes in the cluster morphology.

Acknowledgements

Notes and references

1 U. Heiz, A. Sanchez, S. Abbet and W.-D. Schneider, *J. Am. Chem. Soc.*, 1999, **121**, 3214–3217.
2 M. Mathes, M. Grass, Y. D. Kim and G. Gantefor, *Surf. Sci.*, 2004, **552**, L58–L62.

This journal is © the Owner Societies 2014

Phys. Chem. Chem. Phys., 2014, **16**, 26443–26457 | **26455**

3 S. Vajda, M. J. Pellin, J. P. Greeley, C. L. Marshall, L. A. Curtiss, G. A. Ballentine, J. W. Elam, S. Catillon-Mucherie, P. C. Redfern, F. Mehmood and P. Zapol, *Nat. Mater.*, 2009, **8**, 213–216.

4 M. Arenz, S. Gilb and U. Heiz, *Chem. Phys. Solid Surf.*, 2007, **12**, 1–47.

5 S. Lee, C. Fan, T. Wu and S. L. Anderson, *J. Am. Chem. Soc.*, 2004, **126**, 5682–5683.

6 W. E. Kaden, T. Wu, W. A. Kunkel and S. L. Anderson, *Science*, 2009, **326**, 826–829.

7 A. Boubnov, A. Gaenzler, S. Conrad, M. Casapu and J.-D. Grunwaldt, *Top. Catal.*, 2013, **56**, 333–338.

8 A. Tomita, K.-I. Shimizu, K. Kato, T. Akita and Y. Tai, *J. Phys. Chem. C*, 2013, **117**, 1268–1277.

9 D. N. McCarthy, C. E. Strebel, T. P. Johansson, A. den Dunnen, A. Nierhoff, J. H. Nielsen and I. Chorkendorff, *J. Phys. Chem. C*, 2012, **116**, 15353–15360.

10 X. Chen, J. Chen, Y. Zhao, M. Chen and H. Wan, *Cuihua Xuebao*, 2012, **33**, 1901–1905.

11 G. Busca, E. Finocchio and V. S. Escribano, *Appl. Catal., B*, 2012, **113–114**, 172–179.

12 M. S. Chen, Y. Cai, Z. Yan, K. K. Gath, S. Axnanda and D. W. Goodman, *Surf. Sci.*, 2007, **601**, 5326–5331.

13 E.-Y. Ko, E. D. Park, K. W. Seo, H. C. Lee, D. Lee and S. Kim, *J. Nanosci. Nanotechnol.*, 2006, **6**, 3567–3571.

14 A. K. Santra and D. W. Goodman, *Electrochim. Acta*, 2002, **47**, 3595–3609.

15 K. R. McCrea, J. S. Parker and G. A. Somorjai, *J. Phys. Chem. B*, 2002, **106**, 10854–10863.

16 N. Isomura, X. Wu, H. Hirata and Y. Watanabe, *J. Vac. Sci. Technol., A*, 2010, **28**, 1141–1144.

17 L. Liu, F. Zhou, L. Wang, X. Qi, F. Shi and Y. Deng, *J. Catal.*, 2010, **274**, 1–10.

18 S. Bonanni, K. Ait-Mansour, H. Brune and W. Harbich, *ACS Catal.*, 2011, **1**, 385–389.

19 Y. Watanabe, X. Wu, H. Hirata and N. Isomura, *Catal. Sci. Technol.*, 2011, **1**, 1490–1495.

20 M. J. Berr, F. F. Schweinberger, M. Doeblinger, K. E. Sanwald, C. Wolff, J. Breimeier, A. S. Crampton, C. J. Ridge, M. Tschurl, U. Heiz, F. Jaeckel and J. Feldmann, *Nano Lett.*, 2012, **12**, 5903–5906.

21 S. Bonanni, K. Ait-Mansour, W. Harbich and H. Brune, *J. Am. Chem. Soc.*, 2012, **134**, 3445–3450.

22 M. Moses-DeBusk, M. Yoon, L. F. Allard, D. R. Mullins, Z. Wu, X. Yang, G. Veith, G. M. Stocks and C. K. Narula, *J. Am. Chem. Soc.*, 2013, **135**, 12634–12645.

23 K.-I. Shimizu, K. Ohshima, Y. Tai, M. Tamura and A. Satsuma, *Catal. Sci. Technol.*, 2012, **2**, 730–738.

24 F. J. Perez-Alonso, D. N. McCarthy, A. Nierhoff, P. Hernandez-Fernandez, C. Strebel, I. E. L. Stephens, J. H. Nielsen and I. Chorkendorff, *Angew. Chem., Int. Ed.*, 2012, **51**, 4641–4643.

25 D.-E. Jiang, S. H. Overbury and S. Dai, *J. Phys. Chem. C*, 2012, **116**, 21880–21885.

26 N. Isomura, X. Wu and Y. Watanabe, *J. Chem. Phys.*, 2009, **131**, 164707.

27 H. Yasumatsu, T. Hayakawa and T. Kondow, *J. Chem. Phys.*, 2006, **124**, 014701.

28 R. E. Winans, S. Vajda, G. E. Ballentine, J. W. Elam, B. Lee, M. J. Pellin, S. Seifert, G. Y. Tikhonov and N. A. Tomczyk, *Top. Catal.*, 2006, **39**, 145–149.

29 H. Yasumatsu, T. Hayakawa, S. i. Koizumi and T. Kondow, *J. Chem. Phys.*, 2005, **123**, 124709.

30 d. M. F. Buatier, M. Scherer, B. Gleich, E. Kopatzki and R. J. Behm, *Surf. Sci.*, 1998, **411**, 249–262.

31 K. D. Schierbaum, S. Fischer, M. C. Torquemada, J. L. de Segovia, E. Roman and J. A. Martin-Gago, *Surf. Sci.*, 1996, **345**, 261–273.

32 S. Lee, C. Fan, T. Wu and S. L. Anderson, *J. Chem. Phys.*, 2005, **123**, 124710.

33 W. E. Kaden, W. A. Kunkel and S. L. Anderson, *J. Chem. Phys.*, 2009, **131**, 114701–114715.

34 T. Wu, W. E. Kaden, W. A. Kunkel and S. L. Anderson, *Surf. Sci.*, 2009, **603**, 2764–2770.

35 S. Vajda, S. Lee, K. Sell, I. Barke, A. Kleibert, V. von Oeynhausen, K.-H. Meiwes-Broer, A. F. Rodriguez, J. W. Elam, M. M. Pellin, B. Lee, S. Seifert and R. E. Winans, *J. Chem. Phys.*, 2009, **131**, 121104.

36 W. E. Kaden, W. A. Kunkel, M. D. Kane, F. S. Roberts and S. L. Anderson, *J. Am. Chem. Soc.*, 2010, **132**, 13097–13099.

37 S. Lee, B. Lee, F. Mehmood, S. Seifert, J. A. Libera, J. W. Elam, J. Greeley, P. Zapol, L. A. Curtiss, M. J. Pellin, P. C. Stair, R. E. Winans and S. Vajda, *J. Phys. Chem. C*, 2010, **114**, 10342–10348.

38 W. E. Kaden, W. A. Kunkel, F. S. Roberts, M. Kane and S. L. Anderson, *J. Chem. Phys.*, 2012, **136**, 204705.

39 S. Proch, M. Wirth, H. S. White and S. L. Anderson, *J. Am. Chem. Soc.*, 2013, **135**, 3073–3086.

40 M. D. Kane, F. S. Roberts and S. L. Anderson, *Faraday Discuss.*, 2013, **162**, 323–340.

41 G. Kwon, G. A. Ferguson, C. J. Heard, E. C. Tyo, C. Yin, J. DeBartolo, S. Seifert, R. E. Winans, A. J. Kropf, J. Greeley, R. L. Johnston, L. A. Curtiss, M. J. Pellin and S. Vajda, *ACS Nano*, 2013, **7**, 5808–5817.

42 B.-H. Mao, R. Chang, S. Lee, S. Axnanda, E. Crumlin, M. E. Grass, S.-D. Wang, S. Vajda and Z. Liu, *J. Chem. Phys.*, 2013, **138**, 214304–214311.

43 S. Abbet, A. Sanchez, U. Heiz and W.-D. Schneider, *J. Catal.*, 2001, **198**, 122–127.

44 U. Heiz, A. Sanchez, S. Abbet and W. D. Schneider, *J. Am. Chem. Soc.*, 1999, **121**, 3214–3217.

45 S. Abbet, U. Heiz, H. Häkkinen and U. Landman, *Phys. Rev. Lett.*, 2001, **86**, 5950–5953.

46 L. D. Socaciu, J. Hagen, T. M. Bernhardt, L. Woeste, U. Heiz, H. Haekkinen and U. Landman, *J. Am. Chem. Soc.*, 2003, **125**, 10437–10445.

47 B. Yoon, H. Haekkinen, U. Landman, A. S. Woerz, J.-M. Antonietti, S. Abbet, K. Judai and U. Heiz, *Science*, 2005, **307**, 403–407.

48 C. J. Harding, S. Kunz, V. Habibpour and U. Heiz, *Phys. Chem. Chem. Phys.*, 2008, **10**, 5875–5881.

26456 | *Phys. Chem. Chem. Phys.*, 2014, **16**, 26443–26457

This journal is © the Owner Societies 2014

49 C. J. Harding, S. Kunz, V. Habibpour and U. Heiz, *Chem. Phys. Lett.*, 2008, **461**, 235–237.

50 C. J. Harding, S. Kunz, V. Habibpour, V. Teslenko, M. Arenz and U. Heiz, *J. Catal.*, 2008, **255**, 234–240.

51 S. Kunz, F. F. Schweinberger, V. Habibpour, M. Rottgen, C. Harding, M. Arenz and U. Heiz, *J. Phys. Chem. C*, 2010, **114**, 1651–1654.

52 D. R. Rainer, M. Koranne, S. M. Vesecky and D. W. Goodman, *J. Phys. Chem. B*, 1997, **101**, 10769–10774.

53 M. Valden, X. Lai and D. W. Goodman, *Science*, 1998, **281**, 1647–1650.

54 A. Kolmakov and D. W. Goodman, *Surf. Sci.*, 2000, **490**, L597–L601.

55 F. Gao, Y. Wang, Y. Cai and D. W. Goodman, *Surf. Sci.*, 2009, **603**, 9.

56 S. M. McClure and D. W. Goodman, *Chem. Phys. Lett.*, 2009, **469**, 1–13.

57 I. Z. Jones, R. A. Bennett and M. Bowker, *Surf. Sci.*, 1999, **439**, 235–248.

58 J.-H. Fischer-Wolfarth, J. A. Farmer, J. M. Flores-Camacho, A. Genest, I. V. Yudanov, N. Rösch, C. T. Campbell, S. Schauermann and H.-J. Freund, *Phys. Rev. B: Condens. Matter Mater. Phys.*, 2010, **81**, 241416.

59 H. Conrad, G. Ertl and J. Kueppers, *Surf. Sci.*, 1978, **76**, 323–342.

60 T. Engel and G. Ertl, *Chem. Phys. Lett.*, 1978, **54**, 95–98.

61 T. Engel and G. Ertl, *J. Chem. Phys.*, 1978, **69**, 1267–1281.

62 K. J. Boyd, A. Lapicki, M. Aizawa and S. L. Anderson, *Rev. Sci. Instrum.*, 1998, **69**, 4106–4115.

63 P. J. Chen and D. W. Goodman, *Surf. Sci.*, 1994, **312**, L767–L773.

64 S. C. Street and D. W. Goodman, *Chem. Phys. Solid Surf.*, 1997, **8**, 375–406.

65 X. Lai, C. C. Chusuei, K. Luo, Q. Guo and D. W. Goodman, *Chem. Phys. Lett.*, 2000, **330**, 226–230.

66 Y. Wu, E. Garfunkel and T. E. Madey, *Surf. Sci.*, 1996, **365**, 337–352.

67 Y. Wu, E. Garfunkel and T. E. Madey, *J. Vac. Sci. Technol., A*, 1996, **14**, 2554–2563.

68 M. D. Kane, F. S. Roberts and S. L. Anderson, 2014, in preparation.

69 F. S. Roberts and S. L. Anderson, *Rev. Sci. Instrum.*, 2013, **84**, 126101.

70 S. Lee, C. Fan, T. Wu and S. L. Anderson, *Surf. Sci.*, 2005, **578**, 5–19.

71 M. Aizawa, S. Lee and S. L. Anderson, *Surf. Sci.*, 2003, **542**, 253–275.

72 S. Lee, C. Fan, T. Wu and S. L. Anderson, *J. Phys. Chem. B*, 2005, **109**, 11340–11347.

73 P. A. Redhead, *Vacuum*, 1962, **12**, 203–211.

74 C. Fan, T. Wu, W. E. Kaden and S. L. Anderson, *Surf. Sci.*, 2006, **600**, 461–467.

75 S. Lee, C. Fan, T. Wu and S. L. Anderson, *J. Phys. Chem.*, 2005, **109**, 381–388.

76 X. Tong, L. Benz, S. Chretien, P. Kemper, A. Kolmakov, H. Metiu, M. T. Bowers and S. K. Buratto, *J. Chem. Phys.*, 2005, **123**, 204701–204706.

77 X. Tong, L. Benz, P. Kemper, H. Metiu, M. T. Bowers and S. K. Buratto, *J. Am. Chem. Soc.*, 2005, **127**, 13516–13518.

78 S. K. Buratto, M. T. Bowers, H. Metiu, M. Manard, X. Tong, L. Benz, P. Kemper and S. Chretien, *Chem. Phys. Solid Surf.*, 2007, **12**, 151–199.

79 X. Tong, L. B. Benz, P. Kemper, H. Metiu, M. T. Bowers and S. K. Buratto, *Abstracts of Papers, 234th ACS National Meeting, Boston, MA, United States, August 19–23, 2007*, 2007, COLL-202.

80 X. Tong, S. P. Price, C. Ridge, L. B. Benz, P. Kemper, H. Metiu, M. T. Bowers and S. Buratto, *Abstracts of Papers, 237th ACS National Meeting, Salt Lake City, UT, United States, March 22–26, 2009*, 2009, PHYS-416.

81 X. Tong, L. Benz, S. Chretien, H. Metiu, M. T. Bowers and S. K. Buratto, *J. Phys. Chem. C*, 2010, **114**, 3987–3990.

82 F. S. Roberts, M. D. Kane and S. L. Anderson, 2014, unpublished results.

83 R. Schlaf, P. G. Schroeder, M. W. Nelson, B. A. Parkinson, C. D. Merritt, L. A. Crisafulli, H. Murata and Z. H. Kafafi, *Surf. Sci.*, 2000, **450**, 142–152.

84 R. Levy and M. Boudart, *Science*, 1973, **181**, 547–549.

85 J. W. Rabalais, *Principles and applications of ion scattering spectrometry: surface chemical and structural analysis*, Wiley, New York, 2003.

86 W. E. Kaden, W. A. Kunkel, F. S. Roberts, M. Kane and S. L. Anderson, *Surf. Sci.*, 2014, **621**, 40–50.

87 J. Smolanoff, A. Lapicki and S. L. Anderson, *Rev. Sci. Instrum.*, 1995, **66**, 3706–3708.

88 M. Aizawa, S. Lee and S. L. Anderson, *J. Chem. Phys.*, 2002, **117**, 5001–5011.

89 M. D. Kane, F. S. Roberts and S. L. Anderson, 2014, unpublished results.

90 A. Szabó, M. A. Henderson and J. T. Yates Jr, *J. Chem. Phys.*, 1992, **96**, 6191–6202.

91 J. Xu and J. T. Yates Jr, *J. Chem. Phys.*, 1993, **99**, 725–732.

92 J. Xu and J. T. Yates Jr, *Surf. Sci.*, 1995, **327**, 193–201.

93 B. Hammer and J. K. Norskov, *Nature*, 1995, **376**, 238–240.

94 B. Hammer and J. K. Norskov, in *Adv. Catal.*, ed. B. C. Gates and H. Knozinger, Academic Press, 2000, vol. 45, pp. 71–125.

95 C. T. Campbell and J. R. V. Sellers, *Faraday Discuss.*, 2013, **162**, 9.

96 C. T. Campbell, *Acc. Chem. Res.*, 2013, **46**, 1712–1719.

97 T. W. Hansen, A. T. Delariva, S. R. Challa and A. K. Datye, *Acc. Chem. Res.*, 2013, **46**, 1720–1730.

98 J. Zhang and A. N. Alexandrova, *J. Chem. Phys.*, 2011, **135**, 174702.